Multimodal Approach to Monitoring and Investigating Cone Structure and Function in an Inherited Macular Dystrophy

LUCIA ZICCARDI, DANIELA GIANNINI, GIUSEPPE LOMBARDO, SEBASTIANO SERRAO, ROBERTO DELL'OMO, ANNALISA NICOLETTI, MATTEO BERTELLI, AND MARCO LOMBARDO

• PURPOSE: To examine a female subject, her father, and a brother harboring a missense mutation of the retinitis pigmentosa 1-like 1 (*RP1L1*) gene, over 2 years of follow-up.

• DESIGN: Observational case series.

• METHODS: SETTING: Fondazione G.B. Bietti IRCCS, Rome, Italy. STUDY POPULATION: *RP1L1* family members and controls. MAIN OUTCOME MEASURES: Images of the cone mosaic acquired with an adaptive optics retinal camera, spectral-domain optical coherence tomography (SD OCT), and full-field and multifocal electroretinography (mfERG).

• RESULTS: In the proband, best-corrected visual acuity (≤0.7 logMAR) was stable in both eyes during follow-up, though analysis of adaptive optics images showed decreased cone density in the central 9 degrees from the fovea with respect to controls ($P < .05$) and cone density loss in the parafoveal area (2 degrees; < 12%–16%) during follow-up. Texture analysis of SD OCT images identified abnormalities of the ellipsoid zone in the central 7 degrees, while mfERG response amplitudes were reduced only in the central 5 degrees relative to controls. In the proband's father, who had 0.0 logMAR visual acuity, significant cone loss was found in the central 7 degrees from the fovea ($P < .05$); abnormal SD OCT and mfERG values with respect to controls were found in corresponding retinal areas. No defects in the cone structure and function were found in the proband's brother, who had 0.0 logMAR visual acuity.

• CONCLUSIONS: Occult macular dystrophy was diagnosed based on genetic and multimodal ophthalmic findings. The quantitative assessment of photoreceptor survival or loss, based on analysis of adaptive optics retinal images, was valuable to monitor disease progression at a cellular level. (Am J Ophthalmol 2015;160(2): 301–312. © 2015 by Elsevier Inc. All rights reserved.)

O CCULT MACULAR DYSTROPHY IS A RARE MACU-lar dystrophy presenting with progressive bilateral central visual loss, normal fundus appearance, and normal fluorescein angiography even in advanced stages.[1,2] For this reason, occult macular dystrophy has been frequently misdiagnosed as normal-tension glaucoma, retrobulbar optic neuritis, or amblyopia. Several authors have hypothesized that this retinal dystrophy may include various disease entities with different genetic bases and autoimmune pathophysiology.[3–6] Indeed, patients with diagnosis of occult macular dystrophy have shown different clinical and functional signs. Several putative pathogenic variants of the retinitis pigmentosa 1-like 1 (*RP1L1*) gene (p.R45W, p.Arg.45Trp, p.S1199C, p.Gln2311Pro, p.Asp1425His, p.Ser676Cys and p.W960R; available at http://www.ncbi.nlm.nih.gov/projects/SNP/) have been reported in sporadic cases or in families, with autosomal dominant inheritance, in association with the occult macular dystrophy phenotype.[7–13] It is therefore well accepted that several independent mutations can lead to the occult macular dystrophy phenotype (Supplemental Text, available at AJO.com). New questions have arisen around this rare inherited retinal disease: whether 1 or more genes are responsible for the variable phenotype and whether the disease involves only the macula or even larger retinal areas.

In this work, we aim to track structural and functional retinal changes in a young female subject harboring a missense mutation of the *RP1L1* gene over 2 years of follow-up. In addition, her family members underwent genetic and ophthalmic screening.

METHODS

• STUDY POPULATION: A 23-year-old woman (proband) with progressive bilateral visual loss for 6 years was referred to our Clinical Trials Center in September 2012. She had normal ophthalmoscopic findings, normal fluorescein angiography and indocyanine green angiography, normal

fundus autofluorescence, normal full-field electroretinogram for cone and rod components, normal spinocerebral magnetic nuclear resonance imaging, and negative lumbar puncture (to exclude oligoclonal band status for the diagnosis of multiple sclerosis). The proband, her parents (father, 57 years old; mother, 52 years old) and brother (27 years old), and her paternal grandfather (78 years old) were recruited in a study protocol approved by the local Ethical Committee (Azienda Sanitaria Locale Roma A) and gave written informed consent after a full explanation of the procedures. All research procedures described in this work adhered to the tenets of the Declaration of Helsinki.

The proband and her family, except for her grandfather, underwent comprehensive ophthalmologic examination including best-corrected visual acuity (BCVA), contrast sensitivity function testing using a Pelli-Robson chart (Precision Vision, Lasalle, Illinois, USA), full-field electroretinogram (ERG, Erev 2000; Lace Elettronica, Pisa, Italy), multifocal electroretinogram (mfERG; VERIS Clinic 4.9; Electro-Diagnostic Imaging, San Mateo, California, USA) recorded according to International Society for Clinical Electrophysiology of Vision (ISCEV) standards,[14] MP1 microperimetry (Nidek Technologies, Padova, Italy), and ocular biometry using the IOL Master (Carl Zeiss Meditec AG, Hennigsdorf, Germany). Monocular administration of color test was performed using Ishihara pseudoisochromatic plates (24 plates edition, Kanehara Trading Inc, Tokyo, Japan) in natural daylight. An adaptive optics flood illumination retinal camera (rtx1; Imagine Eyes, Orsay, France) was used to acquire images of the photoreceptor mosaic. In addition, combined scanning laser ophthalmoscopy and spectral-domain optical coherence tomography (SD OCT) was performed using a Spectralis device (Heidelberg Engineering GmbH, Heidelberg, Germany); fundus autofluorescence was also acquired with the Spectralis. The proband was evaluated over 2 years of follow-up (from September 2012 to July 2014); her family members underwent ophthalmic examination only in February 2014. Blood samples were collected from the whole family and genomic DNA was extracted from peripheral blood lymphocytes using conventional methodologies for genetic testing.

Five healthy volunteers (age, 23.3 ± 1.2 years) were recruited in the study as controls for adaptive optics and SD OCT data acquired from the proband and her brother. Normative data by Curcio and associates[15] were used as controls for adaptive optics data acquired in the proband's parents. In addition, 2 populations of 5 healthy subjects each (1 population with age ranging from 20 to 30 years and the other with age ranging from 50 to 60 years) were used as controls for multifocal electroretinogram testing. Control subjects had no history of systemic or ocular diseases and no previous eye surgery.

• GENETIC TESTING BY MOLECULAR ANALYSIS: Genomic DNA was isolated from peripheral blood using a commercial kit (QIAGEN Blood Pure Gene Gentra, QIAGEN S.r.l., Milan, Italy). A panel of 61 candidate genes known to be involved in retinal dystrophies was analyzed by next-generation sequencing (NGS; Illumina Inc, Hayward, California, USA). Purified DNA was used to synthesize an NGS library according to the protocol Illumina Custom Amplicon (available at http://products.illumina.com/products/truseq_custom_amplicon.html) and was sequenced on Illumina miSeq with protocol PE 2x250. The reads were aligned to the reference genome (UCSC/hg19) using the software provided by the manufacturer. Post-processing was performed using the Genome Analysis Toolkit (GATK) package.[16,17] Briefly, we performed a local realignment of in-del regions using the indelRealigner tool; the base qualities have been recalculated with the BaseRecalibrator tool and finally the variants have been identified using the UnifiedGenotyper tool (standard parameters). The selection of variants of clinical interest was made using the following filters: (1) variant with minor allele frequency <1%; (2) variant localized in the coding sequence (exon ± 8 nucleotides); (3) variant previously reported in the literature (The Human Gene Mutation Database) as pathogenic; (4) variant type (nonsense, splicing, non-in-frame deletion or insertion > missense > in-frame deletion or insertion); and (5) new missense variant defined as damage in silico predictions (LJBSIFT, POLYPHEN2, LRT, Mutation Taster, MutationAssessor).[18] The selected variant in the RP1L1 gene was confirmed by Sanger sequencing with a CEQ 8000 automated sequencer (Beckman Coulter, Milano, Italy) in the proband and her family members starting from a new genomic DNA extraction.

• ACQUISITION AND ANALYSIS OF ADAPTIVE OPTICS RETINAL IMAGES: The rtx1 was used to acquire images at several retinal locations covering an area of 8 × 20 degrees around the fovea. Each image sequence consisted of 40 frames acquired by illuminating a retinal area subtending 4 degrees of visual angle.[19,20] A proprietary program provided by the manufacturer was used to correct for distortions within frames of the raw image sequence and to register and frame-average in order to produce a final image with enhanced signal-to-noise ratio prior to further analysis, as described in previous studies.[19–22] The final images were montaged with i2k Retina Pro (DualAlign LLC, Clifton Park, New York, USA) using the "retinal montage tool." The corrected magnification factor was calculated for each eye in order to correct for the differences in optical magnification and thus retinal image size between eyes.[19–22]

In the proband, the follow-up adaptive optics montages were aligned to one another using a cross-correlation algorithm in order to determine their relative position displacements using the "template matching plugin" (available at https://sites.google.com/site/qingzongtseng/template-matching-ij-plugin) in Image J (http://imagej.nih.gov/ij, National Institutes of Health, Bethesda, Maryland,
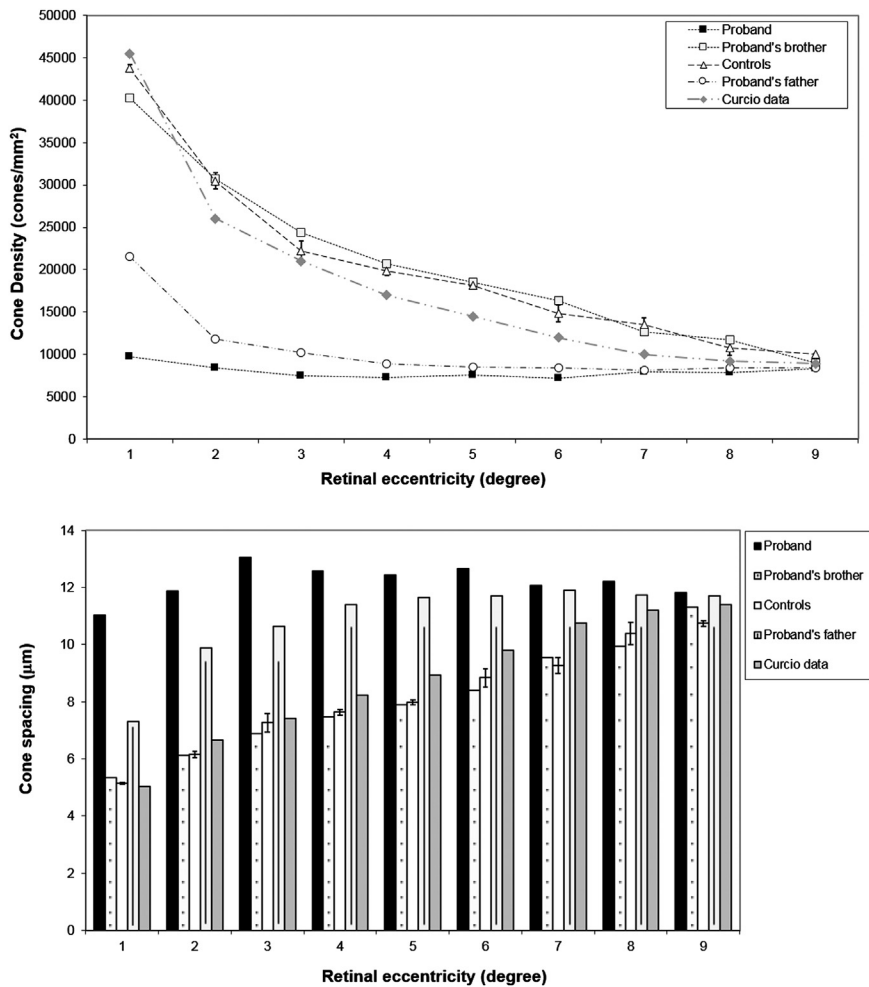
FIGURE 1. Cone density and spacing in a 23-year-old woman with *RP1L1* gene mutation suffering from occult macular dystrophy, her family members, and controls. (Top left) Cone density plotted as a function of retinal eccentricity for the temporal horizontal meridian within 9 degrees of the foveal center. Cone density is shown for the proband (black square), proband's father (white circle), proband's brother (white square), controls (white triangles; bars represent standard deviation), and Curcio's data[15] (gray diamonds). Cone density is significantly reduced in the proband and her father with respect to controls up to 9 and 7 degrees from the fovea, respectively; it is within normal range in the proband's brother. (Bottom left) Histograms of cone spacing plotted as a function of retinal eccentricity for the temporal horizontal meridian within 9 degrees of the foveal center. Symbols are shown in the legend. In the case of controls, the bars represent standard deviation. (Right) The proband (indicated by the arrow), her father, her grandfather, and her brother were all heterozygotes for *RP1L1* gene mutation Arg45Trp. Black fill corresponds to full phenotype, gray fill corresponds to incomplete penetrance.

USA). The baseline image (acquired in September 2012) was used as reference and a template of image features was selected on it in order to improve the alignment algorithm precision. This procedure ensured that the analysis of cone metrics was from exactly the same retinal location at each examination.

The local analysis of density, spacing, and packing arrangements of cones was performed on 64×64-μm sampling areas every 1.0 degree along the temporal meridian, from 1 to 9 degrees from the foveal center. The image cone labeling process was performed using an algorithm implemented with the image processing toolbox in Matlab (The Mathworks Inc, Natick Massachusetts, USA), as previously described.[19–23] After automated cone identification, 2 expert investigators (M.L. and G.L.) reviewed each area and manually identified cones that they agreed to be missed or selected in error by the algorithm. The x-y coordinates of the cones were then used to calculate density, spacing, and packing arrangements of cones. Cone counts were converted into local densities by calculating their number per square millimeter (cones/mm^2). The center-to-center cone distance (μm) was calculated using the nearest-neighbor distance distribution (NND). For each location, the average
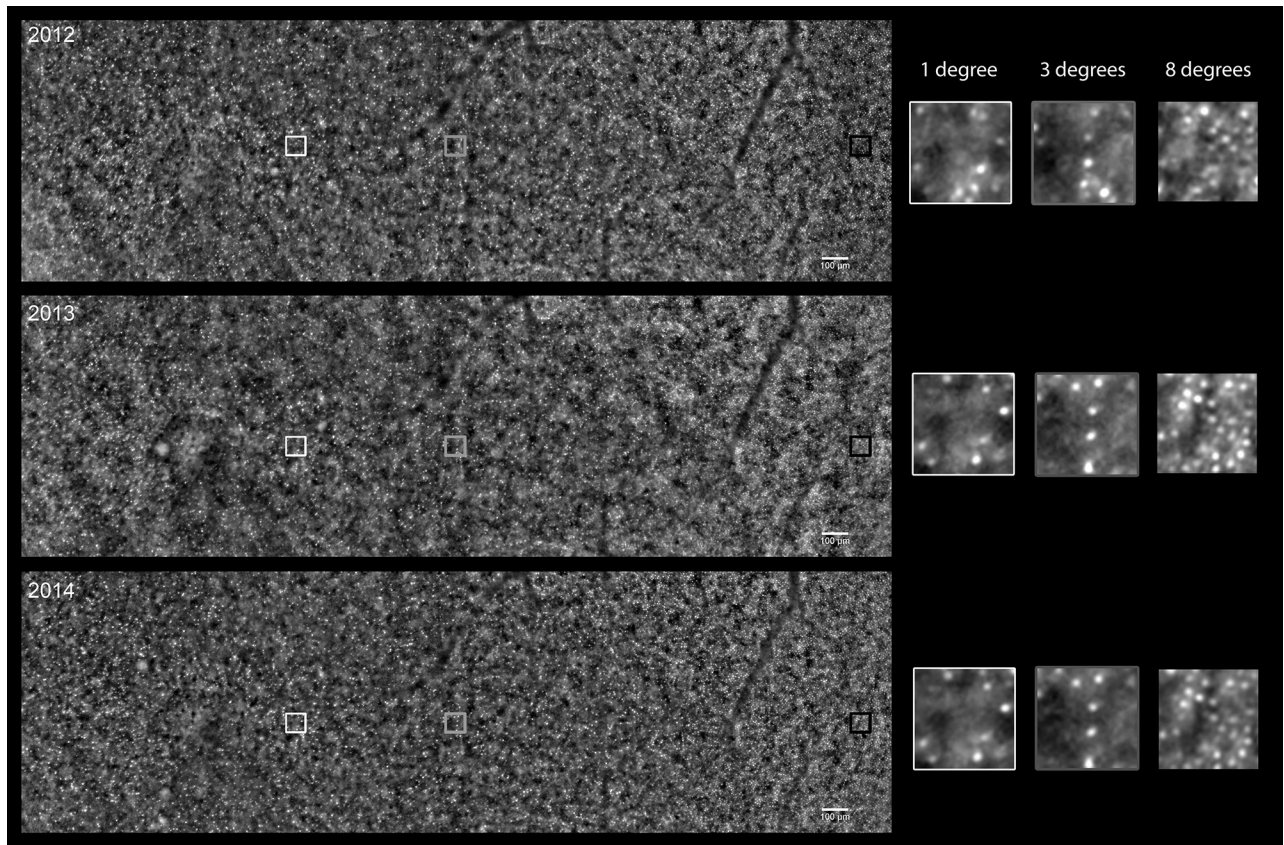
FIGURE 2. Monitoring changes of the cone mosaic over time in a female subject with *RP1L1* mutation suffering from occult macular dystrophy using adaptive optics retinal imaging. (Left) Montages of adaptive optics images of the proband's left eye acquired during follow-up from September 2012 to July 2014 (scale bars: 100 μm). The adaptive optics montages were aligned to one another so that local analysis of cone metrics was from exactly the same retinal location at each examination. The local analysis of density, spacing, and packing arrangements of cones was performed on 64 × 64-μm sampling areas every 1 degree along the temporal meridian. (Right) The insets show the sampling windows (64 × 64 μm) acquired at 1, 3, and 8 degrees temporal to the fovea. Processing and analysis of adaptive optics images permitted accurate tracking of changes of the cone mosaic with cellular resolution over time.

NND was determined by calculating the average of the minimum distances from the center of that cone to the centers of 6 neighboring cones in the mosaic. Voronoi diagrams were computed to analyze the preferred cone packing arrangement, as previously described.[19–21] The Voronoi tessellation was implemented by the Matlab Voronoi function using the x-y centroid coordinates of the labeled cones.

• ACQUISITION AND ANALYSIS OF SPECTRAL-DOMAIN OPTICAL COHERENCE TOMOGRAPHY IMAGES: The SD OCT images were acquired using a volume scan 10 × 15 degrees in the high-resolution modality. In the proband, the SD OCT images were acquired using the "follow-up scan protocol" by Spectralis that automatically aligns the scans across follow-up examinations during acquisition. The baseline scans (September 2012) were used as reference. An automated algorithm was developed in Matlab to segment the SD OCT retinal scans between the external limiting membrane and the inner edge of the retinal pigment epithelium (ie, the interdigitation zone).[24] A thickness map of the photoreceptor layer was developed and its thickness was evaluated across the foveola (0.25 mm diameter) and 3 concentric zones centered on the foveola, such as the parafovea (0.26–1.55 mm), the perifovea (1.56–3.80 mm), and the mid-periphery (3.81–4.20 mm).

Texture analysis of SD OCT scans was performed in order to track potential disruptive changes of the ellipsoid zone during follow-up. This analysis was performed using the Gray Level Co-occurrence Matrix.[25,26] Before calculating the Gray Level Co-occurrence Matrix, each SD OCT image was normalized by histogram equalization. In this study, the Gray Level Co-occurrence Matrix was calculated considering 32 gray levels and 2 specific spatial positions of pairs of neighboring pixels: the horizontal direction (0 degrees)
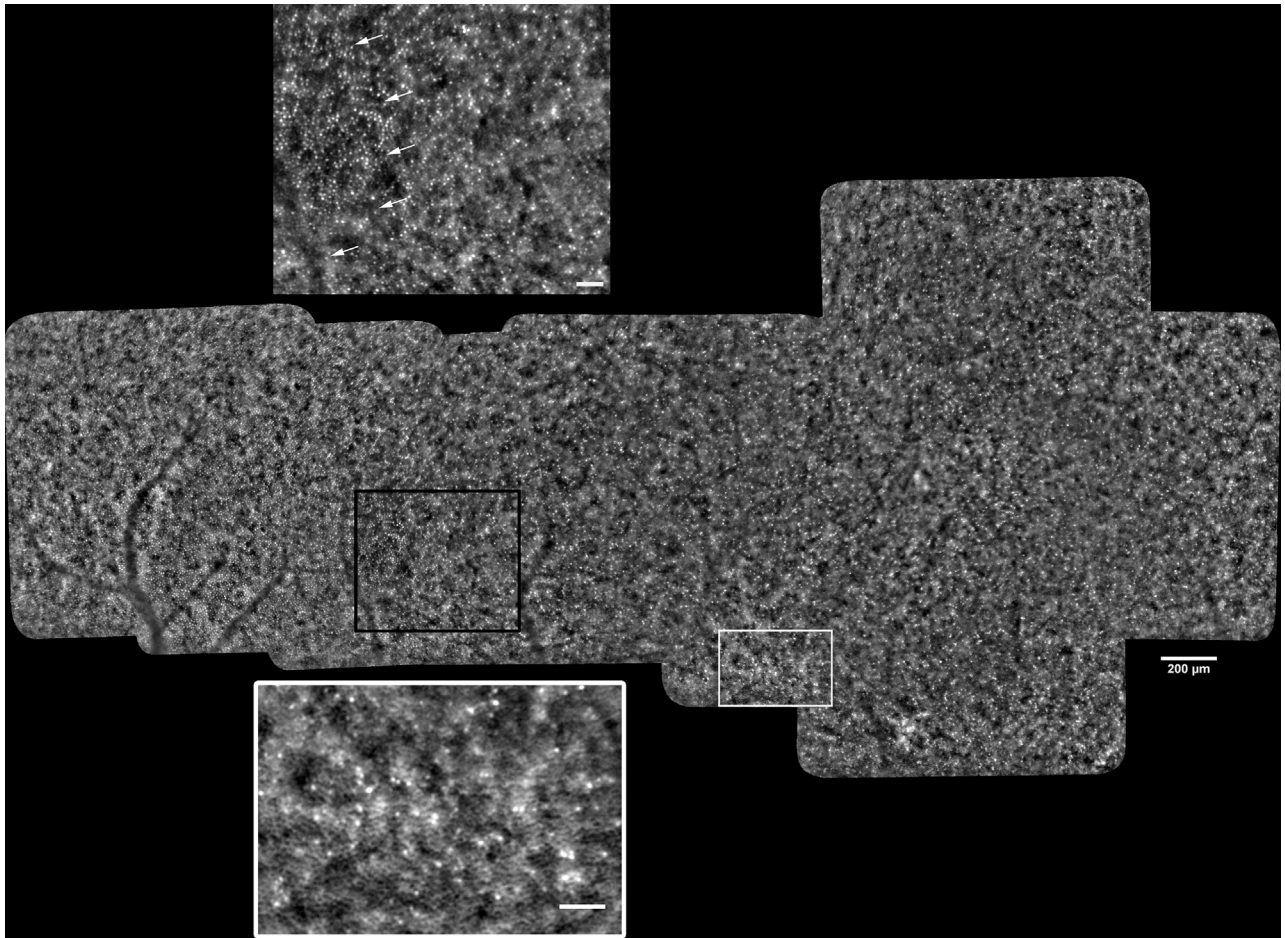
FIGURE 3. Adaptive optics montage showing disruption of the cone mosaic and retinal pigment epithelium cells in a female subject with *RP1L1* gene mutation suffering from occult macular dystrophy. (Top) The white arrows in the black inset shown at Middle (scale bar: 50 μm) indicate a morphologic boundary located at 6 degrees eccentric to the fovea, where the cones start resembling, although not completely, a normal mosaic pattern. (Middle) Montage of adaptive optics images of the proband's right eye acquired in February 2014 (scale bar: 200 μm). The insets highlight 2 regions of interest. (Bottom) The white inset (scale bar: 50 μm) encloses a region of interest showing severe disruption of the cone mosaic; the typical honeycomb retinal pigment epithelial mosaic (mean spacing: 10.3 ± 0.1 μm) can be clearly observed below sporadic bright cones.

and the vertical direction (90 degrees). Thereafter, the correlation was calculated as follows:

$$Correlation = \sum_{i,j} \frac{(i - \mu i) \cdot (j - \mu j) \cdot P_{ij}}{\sigma_i \cdot \sigma_j} \quad (1)$$

where P_{ij} represents the number of occurrences of gray levels i in 1 pixel and j in an adjacent pixel within the region of interest (ROI); μ and σ are the mean and standard deviations of i and j, respectively. The correlation measures how a pixel is correlated with its neighbor over the ROI; in this study, we used the ratio of correlation between 0 degree and 90 degree directions in order to track changes occurring to the ellipsoid zone of the 3 horizontal scans passing through the fovea during follow-up; the lower the value of correlation ratio, the higher the defects of the ellipsoid zone. Texture analysis was performed over the foveola

(0.25 mm) and 3 ROIs across the temporal meridian, thus to be consistent with analysis of adaptive optics data, such as the parafovea (0.26–0.86 mm), the perifovea (0.87–1.99 mm), and the mid-periphery (2.00–2.36 mm).

● ACQUISITION AND ANALYSIS OF MULTIFOCAL ELECTRORETINOGRAM RECORDINGS: The multifocal stimulus, consisting of 61 scaled hexagons, was displayed on a high-resolution, black-and-white monitor (size: 30 × 30 cm) with a frame rate of 75 Hz. The array of hexagons subtended 20 degrees of visual field; each hexagon was independently alternated between black (1 cd/m²) and white (200 cd/m²) according to a binary m-sequence (99% contrast). The luminance of the monitor screen was 100 cd/m². A small red target (0.5 deg) was placed in the center of the stimulation field to maintain a stable fixation and the eye's position
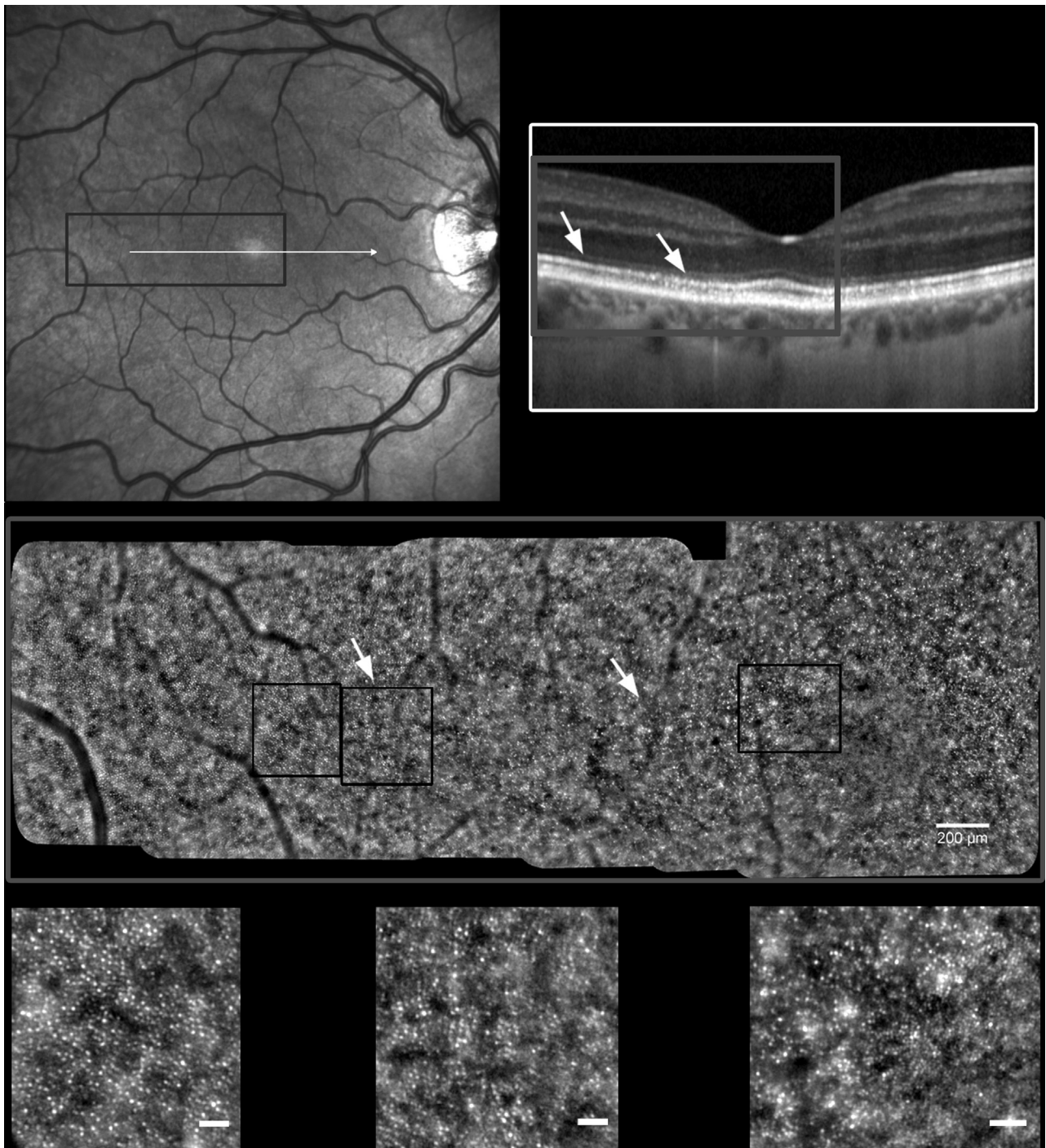
FIGURE 4. Conventional retinal imaging and adaptive optics imaging in an asymptomatic male subject with *RP1L1* gene mutation. (Top left) Scanning laser ophthalmoscopy image of the right eye of the proband's father. The spectral-domain optical coherence tomography (SD OCT) horizontal scan passing through the fovea is highlighted in the gray inset. (Top right) The SD OCT image shows moderate disruption of the ellipsoid zone and blurring of the interdigitation zone in the parafoveal and perifoveal regions (right arrow); the foveola and mid-periphery (left arrow) show normal appearance. The gray insets in the top panels enclose the adaptive optics montage shown in the middle panel. (Middle) Montage of adaptive optics images (scale bar: 200 μm) showing marked disruption of the cone mosaic across the central retina corresponding to disruption of ellipsoid zone in SD OCT image (right arrow). The left arrow indicates the normal structure of the cone mosaic beyond 6 degrees from the fovea. (Bottom left) The inset is centered at 7 degrees eccentric to the fovea; the cone mosaic shows normal arrangement beyond 6 degrees from the fovea. (Bottom middle and Bottom right) Severe disruption of the cone mosaic can be visualized across the central 6.0 degrees. The insets are centered at 6 and 1 retinal degrees, respectively.

|	Right Eye – Temporal Meridian (μm)				Left Eye – Temporal Meridian (μm)				Right Eye – Temporal Meridian (μm)	
	Proband 2012	Proband 2013	Proband 2014_Feb	Proband 2014_Jul	Proband 2012	Proband 2013	Proband 2014_Feb	Proband 2014_Jul	Controls Mean ± SD (95% CI)	Proband's Father
Foveola	69	72	73	71	71	71	75	67	86 ± 1 (86–87)	76
Parafovea	68	69	72	69	70	69	71	64	79 ± 3 (77–81)	76
Perifovea	68	69	70	69	70	69	71	67	74 ± 2 (72–77)	72
Mid-periphery	68	69	69	68	70	68	70	69	71 ± 2 (67–72)	69

Feb = February; Jul = July.
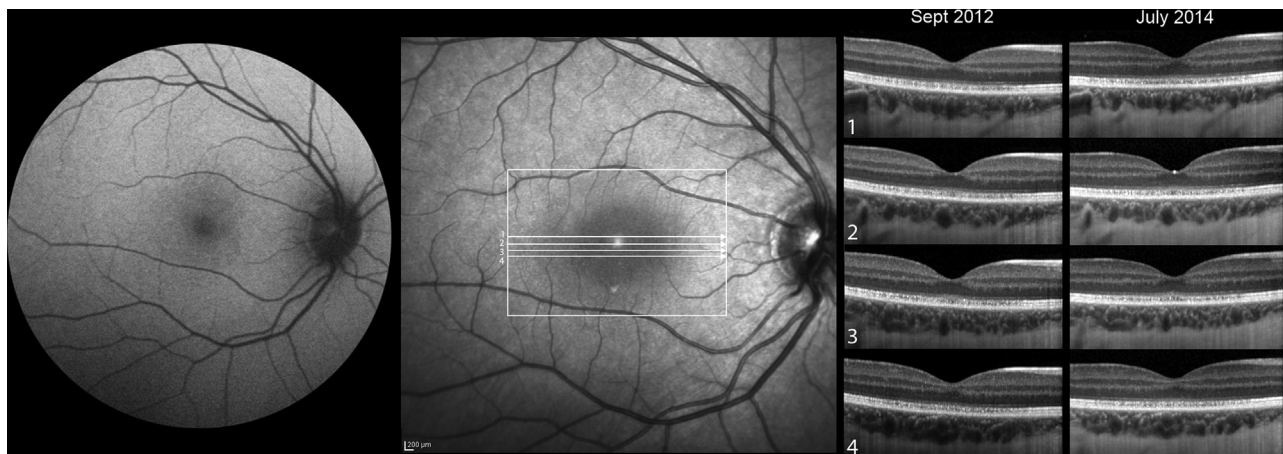
FIGURE 5. Monitoring disease progression with spectral-domain optical coherence tomography (SD OCT) in a female subject with *RP1L1* gene mutation suffering from occult macular dystrophy. (Left) The autofluorescence signal was normal in both eyes of the proband; it did not change during follow-up. Here the autofluorescence image of the right eye is shown. (Middle left) Scanning laser ophthalmoscopy image of the right eye of the proband. The white arrows indicate the SD OCT horizontal scans acquired at baseline (Middle right; September 2012) and at the last examination interval (Right; July 2014). Discontinuities of the ellipsoid zone and blurring of the interdigitation zone in SD OCT images were found in both eyes; any expert grader found clear differences between follow-up scans.

was monitored by a video camera.[27] Trial lenses were used when necessary. The pupils were pharmacologically dilated with 1% tropicamide, the cornea was anesthetized with 1% dicaine, and the mfERGs were recorded binocularly.[27] The mfERGs were recorded between an active electrode (Dawson Trick Litzkow bipolar contact electrode) and a reference electrode (Ag/AgCl skin electrode) placed on the correspondent temporal side of the frontal lobe. An Ag/AgCl skin ground electrode was placed at the center of the forehead (inter-electrode resistance <3 kΩ).

The signal was amplified (gain 100 000) and filtered (band pass 1–100 Hz) by BM 6000 (Biomedica Mangoni, Pisa, Italy). After automatic rejection of artifacts by VERIS Clinic 4.9 software (Electro-Diagnostic Imaging), we examined the first-order kernel response, K1. The mfERG signal-to-noise ratio was estimated following the methodology shown by Hood and Greenstein.[28] In this study, we analyzed the averaged response obtained from 5 concentric annular retinal regions (rings) centered on the foveola. The N1-P1 response amplitude was analyzed from 0 to 2.5 degrees (ring 1, R1), 2.5 to 5 degrees (ring 2, R2), 5 to 10 degrees (ring 3, R3), 10 to 15 degrees (ring 4, R4), and 15 to 20 degrees (ring 5, R5). For each averaged response, we evaluated the response amplitude (nV/deg^2) between the first negative peak, N1, and the first positive peak, P1, and the implicit time (ms) of the first positive peak (P1).

• STATISTICS: Statistical analysis was performed using the SPSS software (version 17.0; SPSS Inc, Chicago, Illinois, USA). The 95% confidence intervals (CI) of control data, defined as mean ± 2 standard deviations, were plotted to define the normal ranges with which to compare SD OCT and mfERG data from the proband and her family members. In the proband, the Steel-Dwass test was used to compare the differences among data acquired at different follow-up examinations and between the proband and controls. The
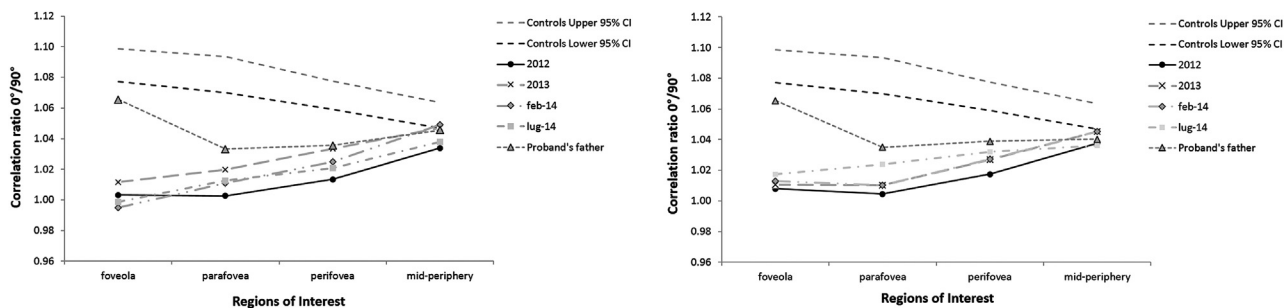
FIGURE 6. Texture analysis of the photoreceptor layer in spectral-domain optical coherence tomography (SD OCT) images of a female subject with *RP1L1* gene mutation suffering from occult macular dystrophy. Texture analysis of SD OCT retinal images was made in order to track changes occurring to the ellipsoid zone during follow-up. The 0 degree/90 degree ratio of correlation is plotted as a function of eccentricity for the temporal horizontal meridian of the right (Left panel) and left (Right panel) eye in study cases and controls, respectively, during follow-up (symbols are shown in the legend). In the proband, the correlation ratios were below the normal range of values for all regions of interest (ROIs), except for the mid-periphery, in which they approached the lower boundary of the 95% confidence intervals (95% CI). The correlation ratios were stable during follow-up. In the proband's father, these parameters were below the 95% CI at all ROIs, though they approached the lower boundary of normal ranges at the foveola and mid-periphery.
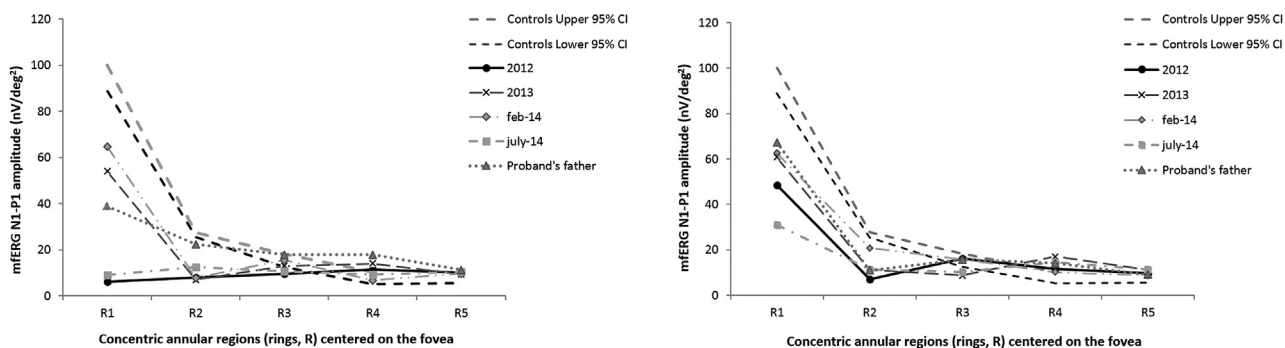

FIGURE 7. Follow-up multifocal electroretinogram recordings in a female subject with *RP1L1* gene mutation suffering from occult macular dystrophy. Response amplitude values of multifocal electroretinograms (mfERG) from 5 rings centered on the fovea (R1-R5) in the right (Left panel) and left (Right panel) eye of the study cases and controls (95% confidence intervals, 95% CI). In the proband, the mfERG showed decreased response amplitude in the central 5 degrees (R1 and R2); after an unexplained improvement in the second and third examinations, the R1-R2 response amplitude returned back to baseline values in both eyes. In the proband's father, the response amplitude values were below the 95% CI of controls in R1 and R1-R2 in the right and left eyes, respectively.

Wilcoxon signed rank test was used to statistically compare the adaptive optics data between the proband's father and Curcio's control data.[15] Differences with a *P* value of .05 or less were considered statistically significant.

RESULTS

AT BASELINE EVALUATION, THE PROBAND'S BCVA WAS 0.7 logMAR in the right eye and 0.7 logMAR − 1 letter in the left eye; the BCVA was stable in the right eye over 2 years of follow-up, but slightly decreased to 1.0 logMAR + 2 letters in the left eye at the last examination; the contrast sensitivity function was 1.50 and 1.35 log

units, respectively, and was stable during follow-up. Indirect ophthalmoscopy, scanning laser ophthalmoscopy, and autofluorescence were normal for both eyes and did not change during follow-up. The microperimetry showed decreased sensitivity (16 dB) within the central 10 degrees in both eyes and was stable during follow-up. The full-field rod and cone electroretinogram was normal in both eyes, and the patient was able to read the 24 Ishihara color plates correctly.

The proband's parents and brother had 0.0 logMAR BCVA and 1.65 log contrast sensitivity function in both eyes; they did not complain of any visual disturbance. The full-field rod and cone responses and the color test were normal in all family members. Parental consanguinity was denied by the patients (Figure 1).
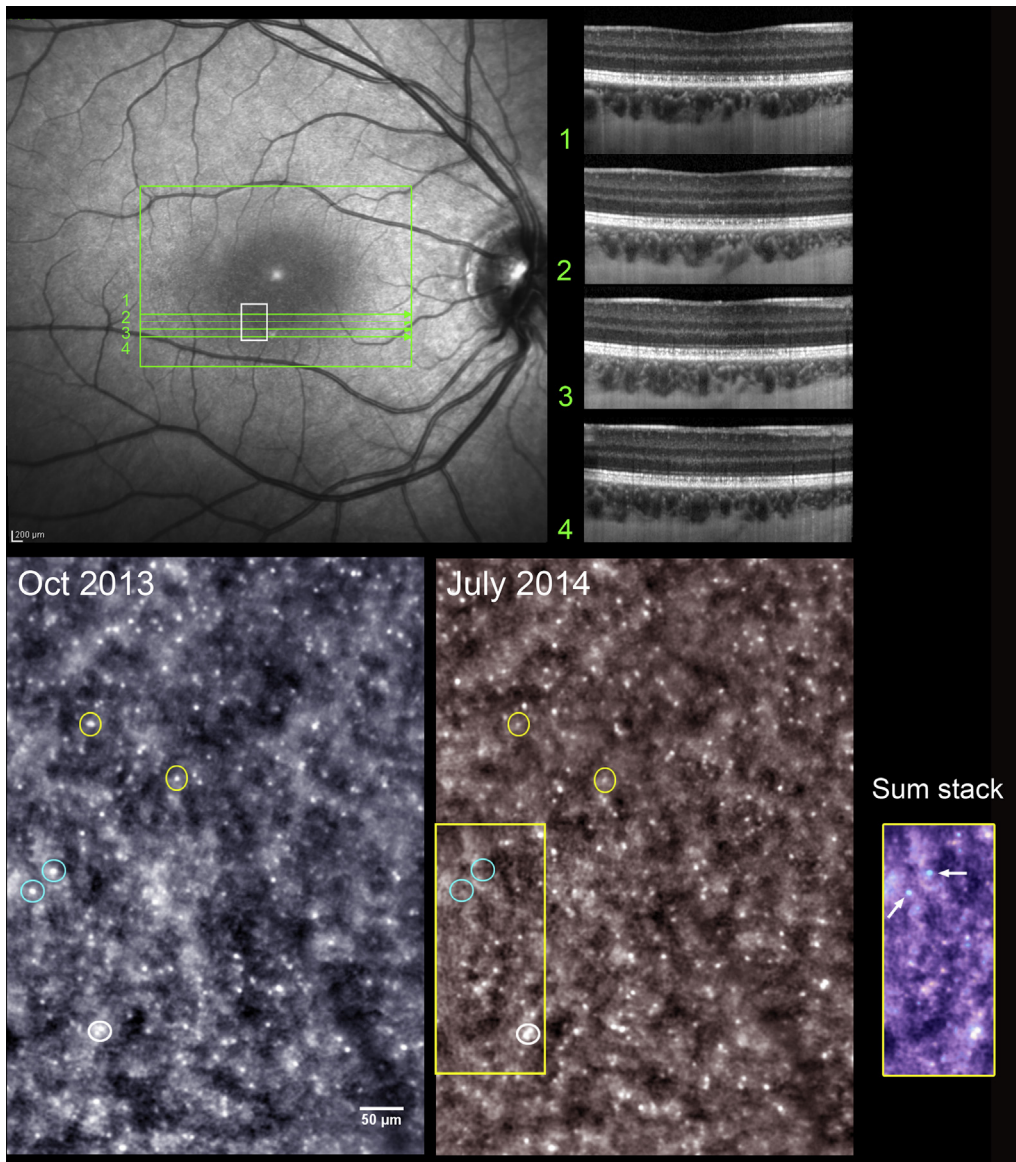
FIGURE 8. Monitoring disease progression in a female subject with *RP1L1* gene mutation suffering from occult macular dystrophy at a cellular level. (Top left) Scanning laser ophthalmoscopy image of the proband's right eye. (Top right) The green arrows indicate the spectral-domain optical coherence tomography horizontal scans acquired at the last examination interval, showing disruption of the ellipsoid zone and blurring of the interdigitation zone. (Bottom left and Bottom right) High-magnification areas from Top left panel (white square; scale bars: 50 μm) showing details of the cone mosaic at 2 examination intervals (October 2013 and July 2014; false color in both panels). The white circle encloses the cones that had stable brightness in adaptive optics flood illumination images over time. The yellow circles enclose the cones that became dimmer over time, likely related to loss of their waveguiding properties caused by outer segment shortening. The blue circles enclose the cones that were lost over time; the retinal pigment epithelial cells could be clearly observed at the same x-y coordinates in the follow-up adaptive optics image. The yellow inset includes the sum stack of the 2 regions of interest. The blue dots (white arrows) represent the cones that were lost during follow-up; the cones with stable brightness over time were represented as white dots.

• **GENETIC ANALYSIS:** In the proband, the next-generation sequencing analysis identified a missense mutation in exon 2 of the *RP1L1* gene: NM_178857:c.133C>T:(p.Arg45Trp); segregation analysis showed that the proband's grandfather, father, and brother had the same heterozygous mutation of the *RP1L1* gene. The transmission pattern in this family was therefore identified as autosomal dominant. The proband's mother did not carry any *RP1L1* gene mutation. The medium coverage in *RP1L1* gene resulted in 329.63 X, with 69.3% of regions with a coverage of at least 25 X. Owing to the presence of several tandem repeats in *RP1L1* exon

4, the following regions were sequenced with a coverage < 10X: RP1L1 (chr8:10464623–10465684), RP1L1 (chr8:10465907–10466076), RP1L1 (chr8: 10466583–10466781 0 X), RP1L1 (chr8:10467401–10467724), RP1L1 (chr8:10468503–10468705), and RP1L1 (chr8:10469889–10470103). The RP1L1 gene mutation (Arg45Trp) was the only variant detected; no other variant was found among the other 60 genes of the panel (Supplemental Table, available at AJO.com), corresponding to the prioritization criteria.

• ADATIVE OPTICS RETINAL IMAGING: In the proband, the cone density was significantly lower than age-matched controls between 1 and 7 degrees from the fovea ($P < .001$), approaching normal values beyond 7 degrees from the fovea in both eyes ($P = .01$; Figure 1). Density ($P > .05$) and spacing ($P > .05$) of cones were stable at all retinal locations in both eyes during follow-up; cone density decreased at 2 degrees from the fovea (<12%–16%) more than at other retinal locations (0–10%) in both eyes during follow-up. Adaptive optics imaging permitted accurate tracking of changes of the cone mosaic at a cellular level (Figure 2). The cone mosaic was severely disrupted across the central retina, showing a normal arrangement beyond 7 degrees from the fovea; the percentage (%) of hexagonal Voronoi tiles ranged between 41% and 27% at 1 and 9 degrees from the fovea, respectively. Cone loss was demonstrated in areas where the retinal pigment epithelium cells could be clearly visualized in adaptive optics images (Figure 3).

The accuracy of the cone identification algorithm in the proband was lower than controls. The mean percentage of manually identified cones was 16% ± 7% and 5% ± 3%, respectively. In the proband, the percentage of unidentified or misidentified cones decreased to control values at 7 degrees from the fovea.

In the proband's father, both density ($P < .01$) and spacing ($P < .01$) values were significantly lower than histologic data by Curcio and associates[15] across the central 7 degrees from the fovea (Figure 1); adaptive optics showed clear disruption of the photoreceptor mosaic in this area (Figure 4). The percentage of hexagonal Voronoi tiles ranged between 51% and 37% at 1 and 9 degrees from the fovea, respectively. In the proband's brother, both cone density and spacing values were within normal values at all areas eccentric to the fovea (Figure 1). Voronoi diagrams were within normal limits, showing an average percentage of hexagonal Voronoi tiles ranging between 54% and 43% at 1 and 9 degrees from the fovea, respectively. The photoreceptor mosaic showed normal structure and morphology.

• SPECTRAL-DOMAIN OPTICAL COHERENCE TOMOGRAPHY IMAGING: In the proband, the average thickness of the photoreceptor layer was below the lower 95% confidence interval of controls in all ROIs, except for the mid-periphery (Table). Differences of less than 5% (≤4 μm) were found at all ROIs in both eyes during follow-up. The SD OCT images showed discontinuities of the ellipsoid zone and blurring of the interdigitation zone in both eyes (Figure 5). The correlation ratio was below the lower 95% confidence interval of controls in all regions of interest, except for the mid-periphery (Figure 6): this region of interest corresponded to 7 degrees eccentric to the fovea. No significant differences between values were found during follow-up ($P > .05$) or between eyes ($P > .05$) in any region of interest.

In the proband's father, the photoreceptor layer was thinner than controls across the foveola and parafovea (Table). The correlation ratios were below the 95% confidence interval of controls in the parafoveal and perifoveal regions of interest; they approached normal values in the foveola and were within normal limits in the mid-periphery (Figure 6). In the proband's brother, both the segmentation data and texture parameters of the photoreceptor layer were within normal limits in all ROIs.

• MULTIFOCAL ELECTRORETINOGRAM RECORDINGS: In the proband, the multifocal electroretinogram N1-P1 response amplitude values were below the lower 95% confidence intervals of controls across the central 2 rings (R1 and R2, for a total of 5 degrees) and relatively well preserved in the retinal periphery (from R3 to R5) in both eyes (Figure 7). The multifocal electroretinogram recordings showed variable response amplitudes in both eyes during follow-up. In the right eye, the R1 N1-P1 response amplitude increased at the second examination with respect to the baseline values (from 6 nV/deg^2 to 54 nV/deg^2). On the other hand, at the last examination (9 nV/deg^2), they returned to baseline values. The fellow eye showed less variability in the response amplitudes during follow-up; however, the R1 response amplitude decreased over 2 years of follow-up. Multifocal electroretinogram P1 implicit times fell within the normal range for all rings in both eyes and were stable during follow-up.

The proband's father showed lower R1 response amplitude in both eyes than controls, whereas the R2 response amplitude values were reduced with respect to controls only in the left eye. The peripheral cone function (from R3 to R5) was within normal limits in both eyes (Figure 7). The R1-R5 P1 implicit time values were within normal limits in both eyes. The proband's brother showed normal R1-R5 N1-P1 response amplitudes and P1 implicit times in both eyes, thus excluding any subclinical dysfunction of cones.

DISCUSSION

IN THIS WORK, WE PRESENTED A MULTIMODAL IMAGING-based approach to monitor and assess objectively the pathologic changes of the cone mosaic in a family affected by a

heterozygous mutation of the *RP1L1* gene (p.Arg45Trp). Adaptive optics retinal imaging provided noninvasive and sensitive information on the pathologic disruption of the cone mosaic, even in the absence of subjective (visual loss) or objective (diagnostic imaging) abnormalities.[29] We found decreased cone density and a number of dark areas across the central retina with several cones showing weak reflectivity in both the proband and her father; this phenomenon has already been associated with abnormal waveguiding properties of the cones, possibly related to changes in length of the outer segments.[30–32] In addition, the longitudinal analysis of adaptive optics images provided evidence on the robustness of the method to track longitudinal changes of the cone mosaic at a cellular level. So far, only histologic studies have demonstrated that photoreceptors either are missing or have shortened and severely distorted outer segments with progression of retinal dystrophies. In this work, we demonstrated that, in adaptive optics flood illumination images, cone loss can be proven if the retinal pigment epithelium cells underlying the previously identified cones are clearly resolved on longitudinal investigation of the same cone mosaic (Figure 8). Nonconfocal, split-detector adaptive optics–scanning laser ophthalmoscopic imaging may assess the photoreceptor disruption earlier than adaptive optics flood illumination imaging by investigating the photoreceptor inner segment with or without the presence of a waveguiding outer segment.[33]

Texture analysis of SD OCT images provided a sensitive biomarker to detect the disruptive changes of the ellipsoid zone in the asymptomatic proband's father and was also reliable to track these pathologic changes longitudinally, as shown in the proband. Strong association was found between data acquired by en face adaptive optics and cross-sectional SD OCT imaging modalities. In the proband, analysis of adaptive optics images showed severe cone loss up to 7 degrees from the fovea; accordingly, texture analysis of the ellipsoid zone in SD OCT images showed abnormal findings up to 7 degrees. Since most of the light coming back from the cone in adaptive optics flood illumination images is scattered back by the ellipsoid zone,[30–32] it is expected that gross alteration to the cone mosaic may be reflected by disruption of the ellipsoid zone in SD OCT images. Previously, the morphologic changes of the ellipsoid and interdigitation zones in patients with occult macular dystrophy have been correlated with disease progression and visual loss.[6,34–36]

Adaptive optics data were moderately associated with measurements of cone dysfunction; the multifocal electroretinogram response amplitudes were lower than controls only in the central 5 degrees. In addition, multifocal electroretinogram recordings showed high variability of measurements during follow-up. These findings may indicate that current functional testing has lower sensitivity than high-resolution imaging techniques in central retinal dystrophies, as previously discussed.[37]

Although occult macular dystrophy has been supposed to be an oligogenic or digenic disease, we did not find any variants in 60 other known genes of retinal dystrophies in this family. The phenotype's heterogeneity in this family was not correlated with age and may involve the potential nocive effect of unknown environmental factors (eg, UV-related photo-oxidation, diet, etc). The different phenotypes in the present family may be ascribed to incomplete penetrance of the R45W variant of the *RP1L1* gene. However, we cannot exclude the possibility that mutations of other genes (not researched in this work) might have contributed to the phenotype.[38]

In conclusion, we described a heterogeneous phenotype consisting of different morphologic and functional abnormalities of central cones across the members of a family harboring a variant of the *RP1L1* gene, known to be associated with occult macular dystrophy. Combining en face and cross-sectional high-resolution retinal imaging data enhances the value of imaging-based ophthalmic diagnostics to monitor disease progression. High-resolution adaptive optics imaging offers new insights into disease progression at a cellular level and can provide a sensitive objective tool to track subtle pathologic changes of photoreceptors on a much shorter time scale than conventional instrumentation.

REFERENCES

1. Miyake Y, Ichikawa K, Shiose Y, Kawase Y. Hereditary macular dystrophy without visible fundus abnormality. *Am J Ophthalmol* 1989;108(3):292–299.
2. Miyake Y, Horiguchi M, Tomita N, et al. Occult macular dystrophy. *Am J Ophthalmol* 1996;122(5):644–653.
3. Piao CH, Kondo M, Tanikawa A, Terasaki H, Miyake Y. Multifocal electroretinogram in occult macular dystrophy. *Invest Ophthalmol Vis Sci* 2000;41(2):513–517.
4. Lyons JS. Non-familial occult macular dystrophy. *Doc Ophthalmol* 2005;111(1):49–56.
5. Sisk RA, Leng T. Multimodal imaging and multifocal electroretinography demonstrate autosomal recessive Stargardt

disease may present like occult macular dystrophy. *Retina* 2014;34(8):1567–1575.

6. Park SJ, Woo SJ, Park KH, Hwang JM, Chung H. Morphologic photoreceptor abnormality in occult macular dystrophy on spectral-domain optical coherence tomography. *Invest Ophthalmol Vis Sci* 2010;51(7):3673–3679.

7. Okuno T, Hayashi T, Sugasawa J, et al. Elderly case of pseudo-unilateral occult macular dystrophy with Arg45Trp mutation in *RP1L1* gene. *Doc Ophthalmol* 2013;127(2):141–146.

8. Tsunoda K, Usui T, Hatase T, et al. Clinical characteristics of occult macular dystrophy in family with mutation of *RP1l1* gene. *Retina* 2012;32(6):1135–1147.

9. Akahori M, Tsunoda K, Miyake Y, et al. Dominant mutations in *RP1L1* are responsible for occult macular dystrophy. *Am J Hum Genet* 2010;87(3):424–429.

10. Ahn SJ, Cho SI, Ahn J, Park SS, Park KH, Woo SJ. Clinical and genetic characteristics of Korean occult macular dystrophy patients. *Invest Ophthalmol Vis Sci* 2013;54(7):4856–4863.

11. Davidson AE, Sergouniotis PI, Mackay DS, et al. *RP1L1* variants are associated with a spectrum of inherited retinal diseases including retinitis pigmentosa and occult macular dystrophy. *Hum Mutat* 2013;34(3):506–514.

12. Kabuto T, Takahashi H, Goto-Fukuura Y, et al. A new mutation in the *RP1L1* gene in a patient with occult macular dystrophy associated with a depolarizing pattern of focal macular electroretinograms. *Mol Vis* 2012;18:1031–1039.

13. Hayashi T, Gekka T, Kozaki K, et al. Autosomal dominant occult macular dystrophy with an *RP1L1* mutation (R45W). *Optom Vis Sci* 2012;89(5):684–691.

14. Hood DC, Bach M, Brigell M, et al. International Society For Clinical Electrophysiology of Vision. ISCEV standard for clinical multifocal electroretinography (mfERG) (2011 edition). *Doc Ophthalmol* 2012;124(1):1–13.

15. Curcio CA, Sloan KR, Kalina RE, Hendrickson AE. Human photoreceptor topography. *J Comp Neurol* 2009;292(4):497–523.

16. Van der Auwera GA, Carneiro M, Hartl C, et al. From FastQ data to high-confidence variant calls: the Genome Analysis Toolkit best practices pipeline. *Curr Protoc Bioinformatics* 2013;11(1110):11.10.1–11.10.33.

17. DePristo MA, Banks E, Poplin R, et al. A framework for variation discovery and genotyping using next-generation DNA sequencing data. *Nat Genet* 2011;43(5):491–498.

18. Liu X, Jian X, Boerwinkle E. dbNSFP: a lightweight database of human nonsynonymous SNPs and their functional predictions. *Hum Mutat* 2011;32(8):894–899.

19. Lombardo M, Serrao S, Lombardo G. Technical factors influencing cone packing density estimates in adaptive optics flood illuminated retinal images. *PLoS One* 2014;9(9):e107402.

20. Lombardo M, Serrao S, Ducoli P, Lombardo G. Influence of sampling window size and orientation on parafoveal cone packing density. *Biomed Opt Express* 2013;4(8):1318–1331.

21. Lombardo M, Serrao S, Ducoli P, Lombardo G. Eccentricity dependent changes of density, spacing and packing arrangement of parafoveal cones. *Ophthalmic Physiol Opt* 2013;33(4):516–526.

22. Lombardo M, Lombardo G, Schiano Lomoriello D, Ducoli P, Stirpe M, Serrao S. Interocular symmetry of parafoveal photoreceptor cone density distribution. *Retina* 2013;33(8):1640–1649.

23. Li KY, Roorda A. Automated identification of cone photoreceptors in adaptive optics retinal images. *J Opt Soc Am A* 2007;24(5):1358–1363.

24. Grzywacz NM, de Juan J, Ferrone C, et al. Statistics of optical coherence tomography data from human retina. *IEEE Trans Med Imaging* 2010;29(6):1224–1237.

25. Haralick RM, Shapiro LG. Computer and Robot Vision. New York: Addison-Wesley Longman Publishing Co; 1992.

26. Gossage KW, Tkaczyk TS, Rodriguez JJ, Barton JK. Texture analysis of optical coherence tomography images: feasibility for tissue classification. *J Biomed Opt* 2003;8(3):570–575.

27. Parisi V, Ziccardi L, Stifano G, Montrone L, Gallinaro G, Falsini B. Impact of regional retinal responses on cortical visually evoked responses: multifocal ERGs and VEPs in the retinitis pigmentosa model. *Clin Neurophysiol* 2010;121(3):380–385.

28. Hood DC, Greenstein VC. Multifocal VEP and ganglion cell damage: applications and limitations for the study of glaucoma. *Prog Retin Eye Res* 2003;22(2):201–251.

29. Ratnam K, Carroll J, Porco TC, Duncan JL, Roorda A. Relationship between foveal cone structure and clinical measures of visual function in patients with inherited retinal degenerations. *Invest Ophthalmol Vis Sci* 2013;54(8):5836–5847.

30. Vohnsen B. Directional sensitivity of the retina: a layered scattering model of outer-segment photoreceptor pigments. *Biomed Opt Express* 2014;5(5):1569–1587.

31. Rativa D, Vohnsen B. Analysis of individual cone-photoreceptor directionality using scanning laser ophthalmoscopy. *Biomed Opt Express* 2011;2(6):1423–1431.

32. Lombardo M, Serrao S, Devaney N, Parravano M, Lombardo G. Adaptive optics technology for high-resolution retinal imaging. *Sensors* 2013;13(1):334–366.

33. Scoles D, Sulai YN, Langlo CS, et al. In vivo imaging of human cone photoreceptor inner segments. *Invest Ophthalmol Vis Sci* 2014;55(7):4244–4251.

34. Ahn SJ, Ahn J, Park KH, Woo SJ. Multimodal imaging of occult macular dystrophy. *JAMA Ophthalmol* 2013;131(7):880–890.

35. Kondo M, Ito Y, Ueno S, Piao CH, Terasaki H, Miyake Y. Foveal thickness in occult macular dystrophy. *Am J Ophthalmol* 2003;135(5):725–728.

36. Brockhurst RJ, Sandberg MA. Optical coherence tomography findings in occult macular dystrophy. *Am J Ophthalmol* 2007;143(3):516–518.

37. Tosha C, Gorin MB, Nusinowitz S. Test-retest reliability and inter-ocular symmetry of multi-focal electroretinography in Stargardt disease. *Curr Eye Res* 2010;35(1):63–72.

38. Audo I, Bujakowska KM, Léveillard T, et al. Development and application of a next-generation-sequencing (NGS) approach to detect known and novel gene defects underlying retinal diseases. *Orphanet J Rare Dis* 2012;7:8.

SUPPLEMENTAL TEXT

OCCULT MACULAR DYSTROPHY (OMD; PHENOTYPE MIM number #613587) has an inherited autosomal dominant trait[1,2]; however, patients with sporadic disease have been also reported.[4,39] Dominant mutations in the *RP1L1* gene were found to be associated with occult macular dystrophy in several Japanese families.[8,9] The *RP1L1* variants have been found also in a Korean population[10] and in few European-descent families.[11] This indicates that inherited occult macular dystrophy is a genetically heterogeneous disorder and that the variants exist on different ethnic backgrounds.

The *RP1L1* gene was cloned as a gene derived from common ancestors of the retinitis pigmentosa 1 (*RP1*) gene, which is responsible for 5%–10% of autosomal dominant retinitis pigmentosa worldwide.[40–43] The 2 genes present sequence similarity owing to the presence of 2 tandem doublecortin (DCX) domains, whose function involves interaction with microtubules.[41] Microtubules are important in allowing nucleokinesis during the mammalian cortical development. Because DCX are a part of the nonclassical microtubule-associated proteins (MAPs),[44] the RP1L1 protein is thought to take the part of microtubule assembly and stabilization in photoreceptor axonemes.[41] In mouse retinal inner segments, the expression of RP1L1 is turned on between prenatal day 15 and birth, a period that coincides with the development of photoreceptors.[41] Based on the colocalization of MAP proteins and their shared microtubule-binding properties, it is likely that RP1L1 shares a function in outer segment morphogenesis and disc stacking.[45] In cynomolgus monkeys, RP1L1 protein resulted to be expressed in both inner and outer segments of rod and cone photoreceptors, and the role of the *RP1L1* gene might be related to photoreceptors' morphogenesis.[40,45] Homozygous *RP1L1* knockout mice showed signs of mild retinal degeneration[45]; however, owing to the very low degree of sequence similarity of the RP1L1 protein between humans and mice, the role of the protein in humans is still under investigation.

Numerous independent *RP1L1* variants can produce the occult macular dystrophy phenotype,[7,9,11–13] and different penetrance of the p.Arg.45Trp mutation has been reported.[9,11] Therefore, occult macular dystrophy has been thought to be not a single gene–causing disease, rather than a digenic or oligodigenic disease.[11] By contrast, Tsunoda and associates[8] have considered this macular dystrophy as different disease entities with similar retinal structural abnormalities and dysfunction. Indeed, macular photoreceptor layer abnormalities have been found in European patients who have been clinically identified as suffering from occult macular dystrophy, although with no mutations of the *RP1L1* gene.[46] The age of onset of occult macular dystrophy phenotype associated to mutations of the *RP1L1* gene has been shown to range between 7 and 75 years.[7,47,48] Overall, these case reports reinforce the opinion that occult macular dystrophy is pathogenetically heterogeneous, suggesting also that nongenetic modifiers, such as environmental or infective or dietary factors, might be involved in the occult macular dystrophy pathophysiology.

Disease progression and severity depending on the genetic trait should be further investigated. Different genotypes of this disease showed different rates of progression.[11] Since the p.R45W mutation has been associated with severe photoreceptoral damage, so far only this variant of the *RP1L1* has been associated with an occult macular dystrophy phenotype of great severity.[10] On the other hand, the p.R45W variant has been described to be the most common genetic mutation of the *RP1L1* gene in Japanese families[11] and there are not yet enough data to claim this conclusion.

In conclusion, there is strong evidence on how several different mutations of the *RP1L1* gene may lead to a disruption of the central cone mosaic up to 10 degrees eccentric to the fovea.[49] Until recently, the conventional ophthalmic imaging instruments (scanning laser ophthalmoscope, autofluorescence, fluorescein angiography, indocyanine green angiography) were unable to detect alterations of the outer retina; spectral-domain optical coherence tomography and especially adaptive optics retinal imaging are, however, sensitive probes from which objective biomarkers of photoreceptor disruption can be developed and used to assess and monitor progressive changes over time.

SUPPLEMENTAL REFERENCES

39. Matthews GP, Sandberg MA, Berson EL. Foveal cone electroretinograms in patients with central visual loss of unexplained etiology. *Arch Ophthalmol* 1992;110(11):1568–1570.

40. Conte I, Lestingi M, den Hollander A, et al. Identification and characterisation of the *retinitis pigmentosa 1-like1* gene (*RP1L1*): a novel candidate for retinal degenerations. *Eur J Hum Genet* 2003;11(2):155–162.

41. Bowne SJ, Daiger SP, Malone KA, et al. Characterization of RP1L1, a highly polymorphic paralog of the retinitis pigmentosa 1 (RP1) gene. *Mol Vis* 2003;9:129–137.

42. Sullivan LS, Heckenlively JR, Bowne SJ, et al. Mutations in a novel retina-specific gene cause autosomal dominant retinitis pigmentosa. *Nat Genet* 1999;22(3):255–259.

43. Jacobson SG, Cideciyan AV, Iannaccone A, et al. Disease expression of RP1 mutations causing autosomal dominant retinitis pigmentosa. *Invest Ophthalmol Vis Sci* 2000;41(7):1898–1908.

44. Dijkmans TF, van Hooijdonk LW, Fitzsimons CP, Vreugdenhil E. The doublecortin gene family and disorders of neuronal structure. *Cent Nerv Syst Agents Med Chem* 2010;10(1):32–46.

45. Yamashita T, Liu J, Gao J, et al. Essential and synergistic roles of RP1 and RP1L1 in rod photoreceptor axoneme and retinitis pigmentosa. *J Neurosci* 2009;29(31):9748–9760.

46. Chen CJ, Scholl HP, Birch DG, Iwata T, Miller NR, Goldberg MF. Characterizing the phenotype and genotype of a family with occult macular dystrophy. *Arch Ophthalmol* 2012;130(12):1554–1559.

47. Wang GL, Jiang LB, Zhang XJ, Wang NL. Clinical analysis of occult macular dystrophy. *Zhonghua Yan Ke Za Zhi* 2011; 47(9):820–823.

48. Takahashi H, Hayashi T, Tsuneoka H, et al. Occult macular dystrophy with bilateral chronic subfoveal serous retinal detachment associated with a novel *RP1L1* mutation (p.S1199P). *Doc Ophthalmol* 2014;129(1):49–56.

49. Tojo N, Nakamura T, Ozaki H, Oka M, Oiwake T, Hayashi A. Analysis of macular cone photoreceptors in a case of occult macular dystrophy. *Clin Ophthalmol* 2013;7:859–864.

Biosketch

Dr. Lucia Ziccardi graduated in Medicine and Surgery in 2002. She earned a specialized degree in Ophthalmology in 2006. Since 2007, she has been working at the Fondazione G.B. Bietti. In 2012, she achieved her PhD in "Neurobiology of neurodegenerative diseases and neural development" after working on the *RS1*-knock out mouse model of juvenile X-linked retinoschisis at the Section for Translation and Research in Retinal and Macular Degeneration at the US National Eye Institute.

Biosketch

Dr. Marco Lombardo graduated in Medicine and Surgery in 1999. He was specialized in Ophthalmology in 2003 and earned his PhD in Biomedical and Computer Engineering in 2007. He has been working at Fondazione G.B. Bietti since January 2010. He is principal investigator in projects related to the clinical application of adaptive optics, the development of new treatment options for keratoconus and the design of novel regenerative therapies using corneal limbal stem cells.

No.	Gene	OMIM ID	Ref Sequence[a]
1	ABCA4	*601691	NM_000350
2	AIPL1	*604392	NM_001285399, NM_001033055, NM_001285403, NM_001285402, NM_001285401, NM_001285400, NM_001033054, NM_014336
3	BBS1	*209901	NM_024649
4	BBS10	*610148	NM_024685
5	BEST1	*607854	NM_001139443, NM_004183
6	C1QTNF5	*608752	NM_015645, NM_001278431
7	CACNA1F	*300110	NM_001256789, NM_001256790, NM_005183
8	CEP290	*610142	NM_025114
9	CHM	*300390	NM_000390, NM_001145414
10	CNGA1	*123825	NM_001142564, NM_000087
11	CNGA3	*600053	NM_001298, NM_001079878
12	CNGB3	*605080	NM_019098
13	CRB1	*604210	NM_201253, NM_001193640, NM_001257965, NM_001257966
14	CRX	*602225	NM_000554
15	CYP1B1	*601771	NM_000104
16	EFEMP1	*601548	NM_001039349, NM_001039348
17	ELOVL4	*605512	NM_022726
18	EYS	*612424	NM_001142800, NM_198283, NM_001142801, NM_001292009
19	FAM161A	*613596	NM_001201543, NM_032180
20	FLVCR1	*609144	NM_014053
21	FZD4	*604579	NM_012193
22	GUCY2D	*600179	NM_000180
23	IMPDH1	*146690	NM_001142573, NM_000883, NM_183243, NM_001102605, NM_001142576, NM_001142575, NM_001142574
24	IQCB1	*609237	NM_001023570, NM_001023571
25	KCNV2	*607604	NM_133497
26	KLHL7	*611119	NM_018846, NM_001031710, NM_001172428
27	LRAT	*604863	NM_004744
28	LRP5	*603506	NM_002335, NM_001291902
29	MYOC	*601652	NM_000261
30	NDP	*300658	NM_000266
31	NR2E3	*604485	NM_016346, NM_014249
32	NRL	*162080	NM_006177
33	NYX	*300278	NM_022567
34	OPA1	*605290	NM_130835, NM_130831, NM_015560, NM_130832, NM_130836, NM_130833, NM_130837, NM_130834
35	OPTN	*602432	NM_021980, NM_001008212, NM_001008213, NM_001008211
36	PDE6A	*180071	NM_000440
37	PDE6B	*180072	NM_001145292, NM_001145291, NM_000283
38	PRPF3	*607301	NM_004698
39	PRPF31	*606419	NM_015629
40	PRPF8	*607300	NM_006445
41	PRPH2	*179605	NM_000322
42	RDH12	*608830	NM_152443
43	RHO	*180380	NM_000539
44	RLBP1	*180090	NM_000326
45	ROM1	*180721	NM_000327
46	RP1	*603937	NM_006269
47	RP1L1	*608581	NM_178857
48	RP2	*300757	NM_006915
49	RPE65	*180069	NM_000329
50	RPGR	*312610	NM_000328, NM_001034853
51	RPGRIP1	*605446	NM_020366
52	RS1	*300839	NM_000330
53	SEMA4A	*607292	NM_001193301, NM_001193300, NM_022367, NM_001193302

No.	Gene	OMIM ID	Ref Sequence[a]
54	*SNRNP200*	*601664	NM_014014
55	*TRPM1*	*603576	NM_001252020, NM_002420, NM_001252024, NM_001252030
56	*TSPAN12*	*613138	NM_012338
57	*TTC8*	*608132	NM_001288782, NM_001288781, NM_198309, NM_144596, NM_001288783, NM_198310
58	*TULP1*	*602280	NM_003322, NM_001289395
59	*USH2A*	*608400	NM_206933, NM_007123
60	*VPS13B*	*607817	NM_017890, NM_152564, NM_015243, NM_181661
61	*WDR36*	*609669	NM_139281

[a]NCBI reference sequence database.